applied sciences

MDPI

Article

Source–Load Data-Driven Multi-Objective Siting and Sizing of Distributed Energy Storage in Islanded Microgrids

Jianfang Chen [1], Haijun Yu [2], Tao Zhou [1], Guansen Wang [1], Zhong Wang [1], Jianming Su [1], Yunzhao Wu [3], Guanglin Sha [3], Guangjing Zhou [4,5,*] and Yi Yang [5,*]

[1] State Grid Anhui Electric Power Co., Ltd. Tongling Power Supply Company, Tongling 244099, China; chenjf5613@ah.sgcc.com.cn (J.C.); 18225621071@163.com (T.Z.); wanggs0435@ah.sgcc.com.cn (G.W.); wangz0519@ah.sgcc.com.cn (Z.W.); sujm061x@ah.sgcc.com.cn (J.S.)
[2] Electric Power Research Institute, State Grid Anhui Electric Power Co., Ltd., Hefei 230000, China; yuhj481x@ah.sgcc.com.cn
[3] China Electric Power Research Institute, Beijing 100192, China; wuyunzhao@epri.sgcc.com.cn (Y.W.); shaguanglin@epri.sgcc.com.cn (G.S.)
[4] School of Traffic and Transportation, Lanzhou Jiaotong University, Lanzhou 730070, China
[5] School of Systems Science, Beijing Jiaotong University, Beijing 100044, China
* Correspondence: gjzhou@lzjtu.edu.cn (G.Z.); calcifery@163.com (Y.Y.)

Abstract

The variability of renewable generation and load demand complicates energy storage planning for islanded microgrids, particularly when siting, sizing, operating reliability, and economic performance must be considered simultaneously. This paper proposes a source-load data-driven method for siting and sizing distributed energy storage in an islanded microgrid. An improved grey wolf optimiser-gated recurrent unit (IGWO-GRU) model was developed to forecast photovoltaic output and nodal loads under normal and adverse weather conditions. The forecasts were incorporated into a multi-objective planning model that maximised islanded supply reliability and capacity-normalised discharge throughput while minimising annualised planning and operating cost. Continuous state-of-charge evolution, transitions between grid-connected and islanded operation, nodal-voltage limits, line-loading limits, upstream-grid power exchange, and priority supply to critical loads were explicitly considered. NSGA-III was directly coupled with a pandapower full-chronology AC power-flow model so that every candidate configuration was evaluated from its simulated operating performance. In the synthetic PV–BESS IEEE 33-bus case study, the 1319 h chronological assessment yielded 640 feasible configurations, including 10 non-dominated solutions. For this synthetic case and predefined candidate buses, the results illustrate a chronological planning workflow and quantify conditional trade-offs among annualised cost, islanded supply reliability, and capacity utilisation. They do not establish universal forecasting or optimisation superiority.

Keywords: distributed energy storage; gated recurrent unit; islanded microgrid; multi-objective optimisation; source-load forecasting; storage siting and sizing

Check for updates

Academic Editor: Alessandro Lo Schiavo

Received: 30 September 2026
Revised: 3 November 2026
Accepted: 12 November 2026
Published: 18 November 2026

Copyright: © 2026 by the authors. Licensee MDPI, Basel, Switzerland. This article is an open access article distributed under the terms and conditions of the Creative Commons Attribution (CC BY) license.

1. Introduction

With the rapid deployment of distributed photovoltaics (PV), wind power, and other renewable energy resources on the distribution side, microgrids have become an important technical solution for facilitating local consumption of distributed energy, improving regional power-supply reliability, and enhancing distribution-system resilience [1]. A

microgrid can operate either grid-connected or in islanded mode following an external grid fault or extreme weather event, and a systematic research foundation has been established for islanded operation and control [2]. During islanded operation, however, the microgrid lacks power support from the main grid. Its renewable generation is highly stochastic, variable, and intermittent because it is affected by irradiance, temperature, wind speed, and other factors, while different types of loads exhibit complex temporal patterns. The coupled uncertainties on the source and load sides therefore pose substantial challenges to real-time power balance, voltage stability, and uninterrupted supply to critical loads in an islanded microgrid [3].

Energy storage systems provide rapid bidirectional power regulation and temporal-spatial energy shifting. They can absorb surplus renewable generation and discharge rapidly during power deficits, making them essential for improving supply-demand balance and operational stability in islanded microgrids. Energy storage nevertheless entails high investment costs, and its location and capacity directly affect supply reliability, operating economics, and energy utilisation efficiency. Insufficient capacity cannot sustain critical loads during abrupt PV output reductions or load surges, whereas excessive capacity increases capital and operation and maintenance (O&M) costs and may result in low asset utilisation. Existing studies on energy storage configuration in islanded microgrids have focused primarily on sizing a single storage system [4–7]. In distribution networks with high penetrations of distributed generation, however, storage location also has a pronounced effect on power-flow distribution, network losses, and nodal voltages; location and installed capacity must therefore be optimised jointly as coupled variables [8,9]. Coordinated siting and sizing of distributed energy storage, with simultaneous consideration of storage location, installed capacity, and charge/discharge power, is thus a central planning problem for islanded microgrids.

Related studies provide complementary foundations for this work. Su et al. [8] optimised multiple storage locations and capacities using clustered seasonal scenarios and NSGA-II. Yang et al. [10] addressed distributed storage planning under uncertain islanding duration through robust optimisation and critical-load supply constraints. Murshed et al. [11] linked forecasting with PV/BESS sizing and explicitly investigated outage resilience. More recent studies incorporated SOC dynamics and network constraints into voltage–loss-oriented storage planning [12] and source–load scenario-based allocation [13]. These individual modelling elements are therefore not claimed as new. The present study integrates forecast nodal injections, continuous SOC evolution across operating-mode transitions, and candidate-wise hourly nonlinear AC power-flow evaluation in one planning loop. The objective values and operating-constraint violations returned by that loop guide the multi-objective search. Table 1 summarises the relationship to these studies.

Table 1. Related storage-planning approaches and the scope of the present integration.

Reference	Reported Emphasis	Connection to This Study
Su et al. [8]	NSGA-II storage placement/capacity; clustered seasonal inputs	Prior distributed allocation; the present evaluation follows a continuous operating-mode chronology.
Yang et al. [10]	Robust distributed storage planning with uncertain islanding duration	Prior islanding and critical-load treatment; here feasibility is returned by hourly AC simulation.
Murshed et al. [11]	Forecast-assisted PV/BESS sizing and outage resilience	Prior forecasting–sizing linkage; here predefined-node allocation is coupled to feeder AC constraints.

Table 1. *Cont.*

Reference	Reported Emphasis	Connection to This Study
Zhi et al. [12]	Voltage–loss-oriented storage planning with SOC and network constraints	Prior network-constrained storage allocation; here reliability and mode-transition chronology are evaluated jointly.
Wu et al. [13]	Source–load scenario-based allocation and SOC/network constraints	Prior temporal-scenario planning; here forecast sequences feed each candidate's continuous AC evaluation.

Continuing improvements in microgrid monitoring, metering, and communication systems have generated extensive historical data on PV generation, loads, weather, and node attributes, providing a new basis for data-driven energy storage planning. Deep-learning models such as recurrent neural networks, long short-term memory networks, and gated recurrent units (GRUs) can extract long-term dependencies from power-system time series and have been applied to PV power and load forecasting [14,15]. The GRU has a relatively compact structure, but its forecasting performance is sensitive to the hidden-layer size, learning rate, initial parameters, and other settings; manual trial and error can readily lead to local optima. The grey wolf optimiser (GWO) features a simple structure, few control parameters, and strong global-search capability [16]. Globally optimising key GRU parameters with this class of swarm-intelligence algorithm can improve forecasting accuracy and generalisation [17]. To address premature convergence and entrapment in local optima in high-dimensional search spaces, improved GWO variants incorporating dimension-learning-based search and related mechanisms have achieved markedly better optimisation quality and convergence stability [18], providing the basis for parameter optimisation in the improved grey wolf optimiser-gated recurrent unit model developed here. Existing data-driven studies, however, focus mainly on reducing forecast errors and seldom investigate how forecasts affect storage location, capacity, and islanded supply reliability. Forecasting and storage-planning models therefore remain insufficiently integrated.

Energy storage siting and sizing in an islanded microgrid also involves complex constraints, including chronological state-of-charge (SOC) evolution, nonlinear AC power flow, nodal-voltage and line-capacity limits, priority supply to critical loads, and transitions between grid-connected and islanded operation. Simplified analytical models cannot simultaneously represent storage energy states and distribution-network operating characteristics with sufficient accuracy. Directly coupling a multi-objective optimisation algorithm with a full-chronology AC power-flow model enables objective values and constraint violations to be calculated from the actual operating results of each candidate configuration. NSGA-III uses reference directions to preserve convergence and diversity in the multi-objective solution set and is suitable for analysing trade-offs among supply reliability, economics, and storage utilisation. Latin hypercube sampling improves the coverage of the initial population in the decision space [19]. Existing studies nevertheless provide insufficient joint treatment of source-load forecasting, alternating normal- and adverse-weather scenarios, transitions between grid-connected and islanded operation, and direct optimisation of storage siting and sizing.

Accordingly, this paper proposes a source-load data-driven method for siting and sizing distributed energy storage in an islanded microgrid. First, source-load time-series data are collected across different weather conditions, service areas, and load types. After missing-value treatment, outlier detection, feature screening, and normalisation, an improved grey wolf optimiser-gated recurrent unit (IGWO-GRU) hybrid forecasting model [16,18] is constructed to obtain PV output and nodal-load forecasts under different scenarios. Second, alternating normal and adverse weather and transitions between

grid-connected and islanded operation are considered. A distributed energy storage siting and sizing model is formulated to maximise islanded supply reliability, minimise planning and operating cost, and maximise capacity-normalised discharge throughput, subject to constraints on storage location, capacity and power, continuous SOC evolution, grid-connected PV power, distribution-network power flow, nodal voltage, line loading, upstream-grid exchange power, and priority supply to critical loads. Finally, NSGA-III is directly embedded around a pandapower full-chronology AC power-flow model. Hourly AC power-flow calculations are performed for every candidate generated by the algorithm, and the feasible Pareto front is extracted from the directly calculated objective values and constraint metrics. The main contributions are as follows:

(1) A forecasting-to-planning workflow is implemented in which weather-dependent PV and nodal-load forecasts supply chronological inputs to storage allocation among predefined candidate buses. The contribution concerns the linkage of these stages, rather than a new standalone forecasting or evolutionary algorithm.
(2) A common storage configuration is evaluated through grid-connected, islanded, and post-islanding operation without resetting its SOC. Reliability, annualised planning and operating cost, and capacity-normalised discharge throughput are evaluated jointly with critical-load, voltage, line-loading, inverter, and SOC requirements.
(3) Hourly steady-state AC feasibility evaluation is embedded in the candidate-selection loop. The synthetic IEEE 33-bus case illustrates how this evaluation distinguishes energy-sufficient configurations from configurations that also satisfy the specified network constraints; it does not establish globally optimal siting or universal algorithmic superiority.

The remainder of this paper is organised as follows. Section 2 presents the methodological models, including the source-load forecasting model and the energy storage siting and sizing model. Section 3 describes the proposed forecasting-driven optimisation algorithm. Section 4 presents the numerical experiments and verifies the proposed method. Section 5 discusses the findings and future research, and Section 6 presents the conclusions.

2. Materials and Methods

The proposed source-load data-driven method for siting and sizing distributed energy storage in an islanded microgrid comprises three interconnected stages: source-load data processing and forecasting, storage siting and sizing modelling, and direct multi-objective optimisation.

The first stage uses historical microgrid operating data and sequentially performs missing-value imputation, outlier detection and smoothing, feature screening, and normalisation. An IGWO-GRU hybrid forecasting model is then constructed to produce PV output and nodal-load forecast sequences under different weather scenarios.

The second stage takes these forecasts as inputs and formulates a distributed energy storage siting and sizing model that considers alternating normal and adverse weather and transitions between grid-connected and islanded operation. The objectives are to maximise islanded supply reliability, minimise planning and operating cost, and maximise capacity-normalised discharge throughput, subject to constraints on the number of storage sites, capacity and power limits, continuous SOC evolution, grid-connected PV power, distribution-network power flow, nodal voltage, line loading, upstream-grid exchange power, and priority supply to critical loads.

In the third stage, NSGA-III is directly embedded around the pandapower full-chronology AC power-flow model. Latin hypercube sampling first generates an initial population covering the decision space. A complete chronological power-flow simulation is then performed for every siting and sizing candidate generated by NSGA-III, simulating

hourly weather changes, transitions between grid-connected and islanded operation, storage charging and discharging, and SOC evolution. The three objective values and constraint violations are calculated directly from the simulation results. Finally, the population is iteratively updated through constraint dominance, non-dominated sorting, and reference-direction selection, and the final Pareto front is extracted from all solutions satisfying the operating constraints.

These stages form a complete chain from operating data to planning decisions: source-load forecasts provide continuous chronological inputs for storage planning, pandapower evaluates the actual operating states of each configuration, and NSGA-III searches for the feasible non-dominated approximation obtained within the evaluation budget using directly simulated objective values and constraint metrics.

2.1. Source-Load Data Preprocessing and Feature Construction

Let the microgrid contain the node set I, with a sampling interval of Δt. The raw data include PV power-generation sequences for each service area, load-power sequences for each node, meteorological features (irradiance, temperature, humidity, and wind speed), and node attributes (residential, commercial, or industrial consumption).

Data preprocessing comprises three sequential operations. First, missing values are imputed: segments shorter than a threshold are filled by linear interpolation, whereas longer missing segments are reconstructed from the daily mean profiles of comparable service areas under similar weather. Second, outliers are detected and smoothed: abrupt deviations beyond three standard deviations within a moving window are removed, and measurement noise is suppressed using a moving average. Third, features are screened and standardised: redundant features whose correlation with the forecast target falls below a threshold are removed, categorical features such as time, weather, service-area category, and load type are encoded, and all continuous features are normalised as

$$\tilde{x} = \frac{x - x_{\min}}{x_{\max} - x_{\min}} \tag{1}$$

thereby eliminating the effect of dimensional differences on model-training stability.

Normalisation parameters are fitted exclusively to the training portion of each forecasting task and then applied unchanged to the validation and test portions. Sliding-window samples preserve chronological order. The validation data are used for hyperparameter selection and early stopping; test targets are excluded from these procedures. Meteorological inputs in this synthetic experiment are scenario-provided information. The reported errors are conditional on that information and do not quantify the additional uncertainty of an operational weather-forecast service.

2.2. IGWO-GRU-Based Source-Load Power Forecasting Model

2.2.1. Input and Output Definitions for the Forecasting Tasks

For the PV power forecasting task, the input feature vector for service area i at time t consists of historical generation and current meteorological features:

$$x^{(g)} = \left[P_{t-\Delta t}^{(i)}, P_{t-2\Delta t}^{(i)}, \ldots, P_{t-n\Delta t}^{(i)}, W_t^{(i)}\right] \tag{2}$$

where $P_{t-k\Delta t}^{(i)}$ is the generation of service area i at time $t - k\Delta t$, $W_t^{(i)}$ is the meteorological feature vector at that time, and n is the historical window length. The corresponding output is

$$y^{(g)} = P_t^{(i)} \tag{3}$$

For the load forecasting task, the input features further incorporate node attributes in addition to historical load power and meteorological features:

$$x^{(l)} = \left[L_{t-\Delta t}^{(j)}, L_{t-2\Delta t}^{(j)}, \ldots, L_{t-n\Delta t}^{(j)}, W_t^{(j)}, A^{(j)}\right] \tag{4}$$

where $L_{t-k\Delta t}^{(j)}$ is the load power at load node j at time $t - k\Delta t$, and $A^{(j)}$ is the node-attribute encoding. The output is

$$y^{(l)} = L_t^{(j)} \tag{5}$$

2.2.2. GRU Network Architecture

To capture long-term dependencies in the source-load sequences, a gated recurrent unit is used as the core forecasting architecture [14,15]. The GRU controls the retention and forgetting of historical information through update and reset gates, substantially reducing the number of parameters relative to a long short-term memory network while retaining temporal modelling capability. Its state-update process is described below.

The update gate controls the proportion of the previous hidden state that is retained:

$$z_t = \sigma(W_z \mathbf{x}_t + U_z h_{t-1} + b_z) \tag{6}$$

The reset gate controls the influence of the historical hidden state on the candidate state:

$$r_t = \sigma(W_r \mathbf{x}_t + U_r h_{t-1} + b_r) \tag{7}$$

The candidate hidden state is generated under the control of the reset gate:

$$\tilde{h}_t = \tanh(W_h \mathbf{x}_t + U_h(r_t \odot h_{t-1}) + b_h) \tag{8}$$

The final hidden state combines historical information with the candidate state:

$$h_t = (1 - z_t) \odot h_{t-1} + z_t \odot \tilde{h}_t \tag{9}$$

The forecast is obtained by a linear mapping at the output layer:

$$\hat{y}_t = W_o h_t + b_o \tag{10}$$

where $\sigma(\cdot)$ is the sigmoid activation function, $\odot$ denotes the Hadamard product, $\mathbf{x}_t$ is the current input vector, h_t is the hidden state, and W_*, U_*, and b_* are the weight matrices and bias vectors of the respective gating units. The parameter set to be optimised is denoted by

$$\theta = \{W_z, U_z, b_z, W_r, U_r, b_r, W_h, U_h, b_h, W_o, b_o\} \tag{11}$$

2.2.3. IGWO Optimisation Mechanism

The evaluated IGWO implementation combines the convergence schedule and sinusoidal step-size factor in Equation (19). The convergence schedule shown there is linear, while the sinusoidal coefficient modulates the step size. The baseline comparisons assess the complete forecasting configurations; they do not identify an independent accuracy contribution from either factor. Accordingly, the method is interpreted as a combined search strategy whose comparative performance is task-dependent.

A population H of Np candidate hyperparameter vectors is initialised. The symbol h denotes a search individual, whereas θ in Equations (11) and (21) denotes trainable network weights:

$$H = \left\{h_1, h_2, \ldots, h_{N_p}\right\} \tag{12}$$

Each individual h_k represents a candidate hyperparameter configuration. After training its network weights on the training subset, its fitness is evaluated on the validation subset:

$$\text{Fitness}(h_k) = \text{NRMSE}_{\text{val}}(h_k) \tag{13}$$

Here, $\text{NRMSE}_{\text{val}}$ denotes the validation-set normalised RMSE criterion used consistently within each task. The same normalisation and fitness definition are used for GWO and IGWO within each task. Training samples are used to fit network weights; validation samples are used to select hyperparameters and determine early stopping. The independent test set is used only for final performance reporting.

The three guiding individuals α, β, and δ are selected in ascending order of fitness, and the relative positional differences between the current individual and the guiding individuals are calculated as

$$D_\alpha = |\lambda_t \cdot C_1 \cdot h_\alpha - h| \tag{14}$$

$$D_\beta = |\lambda_t \cdot C_2 \cdot h_\beta - h| \tag{15}$$

$$D_\delta = |\lambda_t \cdot C_3 \cdot h_\delta - h| \tag{16}$$

The three candidate positions are then obtained as

$$X_1 = h_\alpha - a_t \cdot D_\alpha, \quad X_2 = h_\beta - a_t \cdot D_\beta, \quad X_3 = h_\delta - a_t \cdot D_\delta \tag{17}$$

The current individual is updated to the mean of the three positions:

$$h^{(t+1)} = \frac{X_1 + X_2 + X_3}{3} \tag{18}$$

The coefficients C1, C2, and C3 govern the stochastic position updates. Equation (19) specifies the convergence schedule and sinusoidal step modulation used together in the evaluated search strategy.

$$a_t = 2\left(1 - \frac{t}{T}\right), \quad \lambda_t = 1 + 0.5\sin\left(\frac{\pi t}{T}\right) \tag{19}$$

where t is the current iteration and T is the maximum number of iterations.

2.2.4. Training and Forecasting Procedure

After the search, the hyperparameter configuration with the lowest validation fitness is selected:

$$h^* = \text{argmin}_h \text{Fitness}(h) \tag{20}$$

The selected hyperparameters define a GRU whose network weights are learned using gradient descent:

$$\theta^{(t+1)} = \theta^{(t)} - \eta \nabla_\theta L(f_\theta(x), y) \tag{21}$$

After the search, the hyperparameter configuration with the lowest validation fitness is selected. A GRU with this configuration is trained using gradient descent, with validation-based early stopping, to obtain the forecasting weights. This procedure distinguishes hyperparameter search from network-weight learning and uses the same validation criterion in Equation (13) and Algorithm 1. The final trained weight vector is denoted by θ^{**} in Equations (22) and (23).

During forecasting, given future meteorological conditions and historical power sequences, the PV output forecast is

$$\hat{P}_{t+\tau}^{(i)} = f_{\theta^{**}}\left(x_{\text{new}}^{(g)}\right) \tag{22}$$

and the nodal-load forecast is

$$\hat{L}_{t+\tau}^{(j)} = f_{\theta^{**}}\left(x_{\text{new}}^{(l)}\right) \tag{23}$$

All tasks use one-hour-ahead, single-step prediction. The selected historical input windows are 24 h for normal-weather PV, normal-weather load and adverse-weather PV, and 48 h for adverse-weather load. Inputs comprise historical target power, scenario-provided meteorological variables, temporal features and, for load forecasting, the corresponding node attributes. Future target-power observations are not supplied as predictors.

The search variables are the GRU hyperparameters, rather than all recurrent-network weights. The network weights defined in Equation (11) are learned by gradient-based training for each candidate hyperparameter configuration. Table 2 lists the search ranges, and Table 3 gives the selected configurations. Six wolves and ten search iterations are used. During search, each candidate is trained for at most four epochs and ranked by validation-set normalised root mean squared error (NRMSE). The selected configuration is subsequently trained for up to 20 epochs with validation-based early stopping. Standard GWO-GRU and IGWO-GRU use matching initial populations, search spaces and training budgets.

Table 2. GRU hyperparameter search ranges.

Hyperparameter	Search Range
GRU hidden units	16–128, in increments of 8
Number of GRU layers	1–2
Learning rate	10^{-4}–10^{-2}, logarithmic scale
Batch size	16, 32, 64, 128
Historical input window	12, 24, 48 h
Dropout rate	0–0.4
L2 regularisation coefficient	10^{-7}–10^{-3}, logarithmic scale

Table 3. Selected forecasting hyperparameters.

Forecasting Task	Hidden Units	Layers	Learning Rate	Batch Size	Window (h)	Dropout	L2
Normal-weather PV	128	1	0.005207	32	24	0.4000	8.46×10^{-7}
Normal-weather load	40	1	0.003566	32	24	0.1687	1.37×10^{-4}
Adverse-weather PV	32	1	0.000875	16	24	0.0158	3.99×10^{-5}
Adverse-weather load	24	2	0.007842	64	48	0.0645	1.72×10^{-6}

2.3. Distributed Energy Storage Siting and Sizing Model for an Islanded Microgrid

2.3.1. Decision Variables and Operating Scenarios

The planning variables are the installation indicator x_i, installed energy capacity E_i (MWh), and rated active power P_i (MW) at each candidate bus. Hourly charging and discharging powers are outputs of the chronological dispatch procedure, rather than independent siting-and-sizing decisions. For an installed unit, P_i is bounded between 0.20 and 2.20 MW; an uninstalled unit has zero capacity and power. The candidate set contains buses 8, 15, 22, 29, and 33. The resulting site selections are conditional on this predefined set.

The operating scenario is distinguished by the auxiliary binary variable μ_t. $\mu_t = 1$ denotes normal grid-connected operation, during which the distribution network can exchange power bidirectionally with the upstream grid. $\mu_t = 0$ denotes islanded operation after the root-node circuit breaker is opened during adverse weather or an emergency; the system is then disconnected from the main grid and relies solely on internal PV generation and energy storage to maintain power balance. Source-load data for both operating conditions are taken from the forecasts presented in Section 3.

2.3.2. Optimisation Objectives

For the main planning experiment, the three objectives use two distinct time sets: T_{all} denotes the complete 1319 h evaluation chronology, and T_{isl} denotes its islanded hours. The sampling interval is Δt = 1 h. The installed storage set S contains only units with positive installed energy capacity. Reliability and discharge throughput are maximised, whereas annualised planning and operating cost is minimised. In the remaining operating constraints, T denotes the complete evaluation set T_{all}.

Energy not supplied (ENS) is calculated from the difference between requested and actually served load during islanded operation, after chronological dispatch and operating-feasibility evaluation:

$$ENS = \sum_{t \in T_{isl}} (P_{load,t} - P_{served,t}) \Delta t \quad (24)$$

$P_{load,t}$ is the total requested active load and $P_{served,t}$ is the active load actually supplied in hour t; their difference is non-negative. ENS is measured in MWh. The first objective is the dimensionless islanded energy-supply reliability:

$$\max F_1 = 1 - \frac{ENS}{\sum_{t \in T_{isl}} P_{load,t} \Delta t} \quad (25)$$

The second objective is annualised planning and operating cost. It includes annualised initial energy-capacity and power-capacity investment, net electricity purchase/sale cost, and throughput-based operation and maintenance cost:

$$\min F_2 = C_{inv}{}^{ann} + C_{grid}{}^{ann} + C_{OM}{}^{ann} \quad (26)$$

The components are calculated as follows, with costs expressed in RMB/year:

$$C_{inv}{}^{ann} = CRF \sum_{i \in S} 1000 (c_E E_i + c_P P_i) \quad (27)$$

$$C_{grid}{}^{ann} = 1000 \kappa \sum_{t \in T_{all}} \left(c_t{}^{buy} P_t{}^{buy} - c_t{}^{sell} P_t{}^{sell} \right) \Delta t \quad (28)$$

$$C_{OM}{}^{ann} = 1000 \kappa c_{OM} \sum_{i \in S, t \in T_{all}} \left(p_{i,t}{}^{ch} + p_{i,t}{}^{dis} \right) \Delta t \quad (29)$$

The capital recovery factor is $CRF = \frac{r(1+r)^y}{(1+r)^y - 1}$, where r = 0.08 and y = 10 years. The unit investment costs c_E and c_P are expressed in RMB/kWh and RMB/kW, respectively; the factor 1000 converts the installed MWh/MW values to kWh/kW. The annualisation factor κ = 8784/1319 = 6.659591 scales the simulated grid-interaction and throughput costs to the 8784 h reference year. This proportional scaling assumes that the evaluated chronology is representative of annual operation; it is not an empirical estimate of annual outage frequency. The formulation does not explicitly monetise intermediate replacement, cycle-dependent degradation, residual value or end-of-life disposal. Throughput-based O&M cost should not be interpreted as a calibrated degradation cost. The tariffs $c_t{}^{buy}$ and $c_t{}^{sell}$ and the throughput O&M rate c_{OM} are in RMB/kWh; $P_t{}^{buy}$ and $P_t{}^{sell}$ are non-negative imported and exported powers in MW.

The third objective is capacity-normalised AC discharge throughput over the complete evaluation chronology:

$$\max F_3 = \sum_{i \in S} \frac{E_{dis,i}{}^{AC}}{E_i}, E_{dis,i}{}^{AC} = \sum_{t \in T_{all}} \max\left(P_{i,t}{}^{AC}, 0\right) \Delta t \quad (30)$$

$E_{dis,i}{}^{AC}$ is the cumulative AC-side energy discharged by unit i over T_{all}. In this definition, $P_{i,t}{}^{AC}$ is positive for discharge. F_3 sums the individual ratios $E_{dis,i}{}^{AC}/E_i$; it is not the ratio of total system discharge to total installed capacity. No additional efficiency coefficient appears in this objective. The 90% round-trip efficiency instead affects available energy and discharge through the SOC update. A higher F_3 indicates greater discharge turnover per unit of installed capacity, but may also imply greater cycling exposure and degradation risk. It is not physical charging/discharging efficiency and should not be interpreted in isolation as better battery performance.

2.3.3. Constraints

The storage-capacity and installation-count constraints are

$$0 \le E_i \le x_i E_{max}, \forall i \in I \quad (31)$$

$$\sum_{i \in I} x_i \le N \quad (32)$$

where E_{max} is the upper capacity limit of an individual storage system, and N is the maximum number of storage installations.

Hourly operating powers are limited by the installed rated power and the available SOC. Grid-connected charging and discharging cannot exceed P_i. During islanding, scheduled discharge is limited to $0.95P_i$ to retain a power-regulation margin. Actual AC outputs, including the reference BESS output, are checked against rated active power and the inverter apparent-power limit of $1.20P_i$. The chronological controller also limits aggregate grid-side charging to 3.000 MW in this case.

$$0 \le p_{i,t}{}^{ch} \le P_i, 0 \le p_{i,t}{}^{dis} \le P_i, i \in S, t \in T_{all} \quad (33)$$

$$0.12E_i \le S_{i,t} \le 0.90E_i, i \in S, t \in T_{all} \quad (34)$$

$$S_{i,t+1} = S_{i,t} + \eta_{ch} p_{i,t}{}^{ch} \Delta t - \frac{p_{i,t}{}^{dis} \Delta t}{\eta_{dis}} \quad (35)$$

$S_{i,t}$ is stored energy (MWh), $SOC_{i,t} = S_{i,t}/E_i$, and $\Delta t = 1$ h. The charging and discharging efficiencies are $\eta_{ch} = \eta_{dis} = \sqrt{0.90} = 0.948683$. The final operating constraint is $0.12 \le SOC_{i,t} \le 0.90$, with initial SOC 0.90. Charging and discharging are mutually exclusive: $p_{i,t}{}^{ch}\, p_{i,t}{}^{dis} = 0$. The dispatch logic first determines whether charging is permitted; discharging is considered only when charging is zero and a net-load deficit requires support. SOC is propagated continuously across weather and connection-mode transitions, with actual AC power used for the operating-limit checks. In Equation (35), $p_{i,t}{}^{ch}$ and $p_{i,t}{}^{dis}$ denote the non-negative AC-side powers used in the storage energy balance, including the reference-unit adjustment from the AC solution.

The active-, reactive-, and apparent-power constraints for grid-connected PV are

$$0 \le p_{i,t}^{pv} \le p_{i,t}^{pv\max}, \quad -p_{i,t}^{pv} \tan\beta \le q_{i,t}^{pv} \le p_{i,t}^{pv\max} \tan\beta, \quad \forall t \in T, i \in I \quad (36)$$

$$\| p_{i,t}^{pv}, q_{i,t}^{pv} \| \le S_{i,t}^{pv}, \quad \forall t \in T, i \in I \quad (37)$$

where $p_{i,t}^{pv\max}$ is the maximum available power of the PV node i at time t, as provided by the forecasting model in Section 3; β is the power-factor angle; and $S_{i,t}^{pv}$ is the apparent-power rating of the inverter.

Distribution-network power flow is represented using the DistFlow model for radial networks [20]:

$$P_{ij,t} = p_{j,t} + \sum_{k:j\to k} P_{jk,t} + R_{ij} I_{ij,t}^2, \quad \forall t \in T, i, j \in I \tag{38}$$

$$Q_{ij,t} = q_{j,t} + \sum_{k:j\to k} Q_{jk,t} + X_{ij} I_{ij,t}^2, \quad \forall t \in T, i, j \in I \tag{39}$$

$$\left|V_{j,t}\right|^2 = |V_{i,t}|^2 - 2\left(R_{ij}P_{ij,t} + X_{ij}Q_{ij,t}\right) + \left(R_{ij}^2 + X_{ij}^2\right) I_{ij,t}^2, \quad \forall t \in T, i, j \in I \tag{40}$$

The safety limits on nodal voltage and branch current are

$$V_{\min} \le V_{i,t} \le V_{\max}, \quad \forall t \in T, i \in I \tag{41}$$

$$0 \le I_{ij,t} \le I_{\max}, \quad \forall t \in T, i, j \in I \tag{42}$$

where $P_{ij,t}$ and $Q_{ij,t}$ are the active and reactive powers on branch ij, respectively; R_{ij} and X_{ij} are the branch resistance and reactance; $I_{ij,t}$ is the branch current; $V_{i,t}$ is the nodal voltage; and $p_{j,t}$ and $q_{j,t}$ are the active and reactive nodal loads provided by the forecasting model.

The constraint on power exchange with the upstream grid is

$$p_t^H = \sum_{j\in\delta(1)} P_{1j,t}, \quad q_t^H = \sum_{j\in\delta(1)} Q_{1j,t}, \quad \forall t \in T \tag{43}$$

$$\| p_t^H, q_t^H \| \le \mu_t S_T, \quad \forall t \in T \tag{44}$$

where $\delta(1)$ is the set of nodes directly connected to the root node, and S_T is the capacity of the root-node substation. When $\mu_t = 0$, this constraint automatically forces the exchanged power to zero, thereby representing transitions between grid-connected and islanded operation in a unified mathematical form.

Load-supply priority constraints are specified according to node criticality as

$$\mu_t p_{i,t}^{nom} \le p_{i,t} \le p_{i,t}^{nom}, \quad \mu_t q_{i,t}^{nom} \le q_{i,t} \le q_{i,t}^{nom}, \quad \forall i \in \Theta_g, t \in T \tag{45}$$

$$p_{i,t} = p_{i,t}^{nom}, \quad q_{i,t} = q_{i,t}^{nom}, \quad \forall i \in \Lambda, t \in T \tag{46}$$

where Θ_g and Λ are the sets of general-load and critical-load nodes, respectively, and $p_{i,t}^{nom}$ and $q_{i,t}^{nom}$ are the rated nodal powers. During islanded operation, general loads may be curtailed as required to maintain power balance, whereas critical loads remain fully supplied throughout the islanded period.

During grid-connected operation, the upstream connection at bus 1 supplies the voltage and phase-angle reference, with voltage magnitude 1.025 p.u. During islanding, that connection is opened, and its power exchange is zero. An installed BESS supplies the islanded reference, with priority order 33, 15, 22, 29, and 8 and reference voltage magnitude 1.030 p.u. Other storage units operate as PQ nodes with scheduled injections. The reference BESS accommodates the residual active and reactive imbalance, including network losses, subject to its active-power and inverter apparent-power limits; any violation renders the configuration infeasible rather than being supplied by the disconnected upstream grid. This is a steady-state grid-forming representation, not a model of transient control, frequency dynamics, black start, or protection coordination.

3. Source-Load Forecasting-Driven Distributed Energy Storage Siting and Sizing Algorithm for an Islanded Microgrid

A coordinated source-load forecasting and simulation-based optimisation framework is developed for the source-load data-driven storage siting and sizing problem. IGWO-GRU first forecasts PV output and load power under normal and adverse weather to form chronological source-load scenarios. The forecasts are then input to a pandapower microgrid model, and NSGA-III generates candidate storage siting and sizing solutions. For each candidate, pandapower simulates normal operation and fault-induced islanding and directly calculates the objective values and constraint violations. NSGA-III updates the population from the simulation results and ultimately obtains the feasible non-dominated approximation within the evaluation budget. The framework is shown in Figure 1.

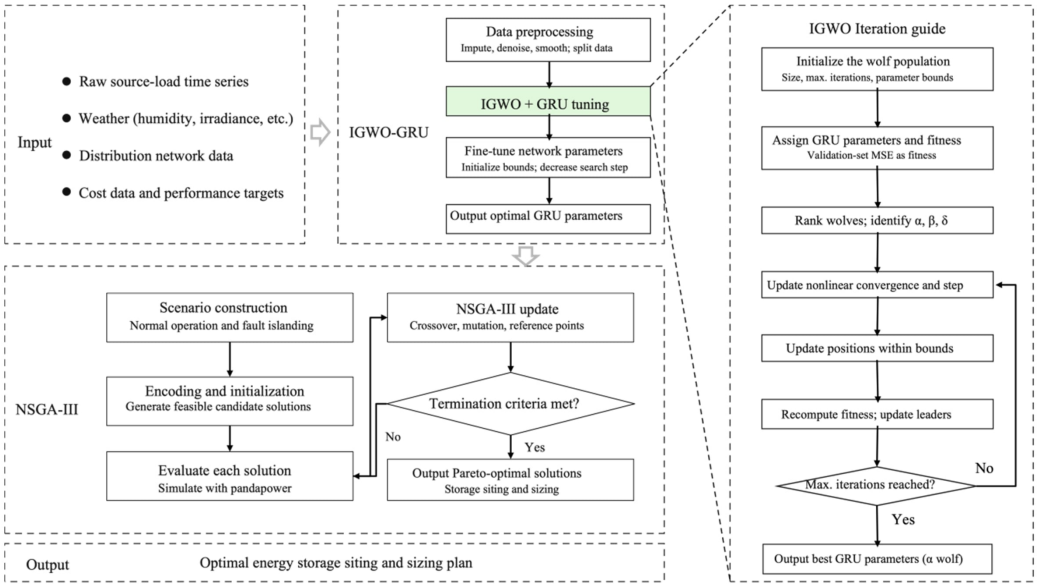


Figure 1. Source-load forecasting-based optimisation framework.

3.1. IGWO-GRU Hybrid Forecasting Algorithm

The forecasting module uses distinct PV and load feature sets and a GRU temporal model. The same chronological partition and evaluation criteria are used when comparing complete forecasting configurations. Meteorological covariates are supplied by the constructed scenarios, and performance claims are restricted to those inputs.

IGWO searches the reported GRU hyperparameter space using the common validation criterion. Its convergence schedule and sinusoidal step modulation are evaluated as a combined search strategy; no improvement is assigned to an individual factor from the aggregate benchmark alone.

After hyperparameter selection, network weights are fitted by gradient descent with validation-based early stopping. Algorithm 1 distinguishes model training, validation-based selection, and independent test evaluation. Comparative performance is quantified in Section 4.2 rather than assumed from the optimisation mechanism.

Algorithm 1. IGWO-GRU Hybrid Prediction Algorithm

Input: chronological synthetic PV/load, meteorological and node features
Output: one-hour-ahead forecasts and test-set error metrics
1. Split the chronology into 6148 training, 1317 validation and 1319 test hours.
2. Fit preprocessing and normalisation on the training subset; construct chronological windows.
3. Initialise six candidate hyperparameter configurations within Table 2 bounds.
4. For each of ten search iterations, train each candidate for at most four epochs on training data and evaluate validation NRMSE.
5. Update the guiding wolves and candidate hyperparameters using the combined schedule and step factor in Equation (19); enforce bounds.
6. Select the lowest-validation-fitness configuration; train its GRU for up to 20 epochs using validation-based early stopping.
7. Predict the independent test targets and report inverse-transformed RMSE, MAE and R^2.
8. Use five independent training runs to summarise the learning-based model comparisons.

3.2. NSGA-III for Energy Storage Siting and Sizing

An AC power-flow model of the distribution network is established in pandapower, with storage installation status, rated capacity, and rated power as the principal decision variables. The same siting and sizing configuration is used to continuously simulate normal weather, adverse weather, grid-connected operation, and islanded operation. During the full-chronology simulation, the corresponding PV and load forecasts are selected according to the hourly weather flag and network operating state. Storage charging/discharging dispatch and SOC updates are performed, and an AC power-flow calculation is run in every period to obtain nodal voltages, line loadings, storage SOC, upstream-grid exchange power, and supplied load. Storage SOC is propagated continuously throughout the chronology and is not reset when weather or grid-connection status changes, thereby representing the energy-support capability of a storage configuration under continuous operation.

NSGA-III is embedded around the full-chronology AC power-flow evaluation. It maximises islanded supply reliability F_1 and capacity-normalised discharge throughput F_3 while minimising annualised planning and operating cost F_2. F_3 is the sum of node-level discharge-to-capacity ratios, not a ratio of system totals or a physical conversion efficiency. The operating constraints cover site count, capacity and power bounds, SOC, nodal voltage, line loading, critical-load supply, general-load supply, and overall islanded reliability.

NSGA-III receives the minimisation vector $(-F_1, F_2/10^6, -F_3)$. The cost scaling changes only its numerical magnitude, not its units when reported or the Pareto-dominance relationships. Results are reported using the original physical objectives. The same objective directions are used when extracting the feasible non-dominated set and when normalising objectives for HV and IGD.

NSGA-III selects individuals through constraint dominance, non-dominated sorting, and reference directions, and generates the next population through crossover, mutation, and variable repair. Upon reaching the maximum number of iterations, non-dominated solutions are extracted from all feasible configurations evaluated using full-chronology power flow to form the Pareto front for storage siting and sizing.

The main planning search uses a population of 32 and 20 generations, giving a budget of 640 candidate evaluations. Simulated binary crossover uses probability 0.90 and distribution index 15; polynomial mutation uses a per-variable probability of 1/16 and distribution index 20. Three-objective Das–Dennis reference directions use six partitions.

The reported comparison used Python 3.13.2, pymoo 0.6.2 and pandapower 3.5.4 on an Apple M2 Mac mini with 8 GB memory and eight parallel processes. The algorithm for the simulation-based optimization model is presented in Algorithm 2.

Algorithm 2. Simulation-Based Optimisation Framework

Input: Source-load prediction scenarios, weather and network-state sequence, candidate storage nodes, capacity and power bounds, distribution-network parameters, operational constraints, and NSGA-III parameters
Output: Feasible non-dominated storage siting, capacity, and power configurations
1. Optimisation Model Initialisation
Define installation, energy-capacity and rated-power variables $x = \{x_{i,E}_i, P_i\}$.
Define the optimisation objectives:
F1: maximise islanded power supply reliability
F_2: minimise annualised planning and operating cost
F3: maximise capacity-normalised discharge throughput
Define the constraints on storage quantity, capacity, power, SOC, node voltage, line loading, critical-load supply, and general-load supply

2. NSGA-III Population Initialisation
Generate the NSGA-III reference directions
Generate the initial population using Latin hypercube sampling
Add representative boundary configurations to the initial population
Repair each individual to satisfy the variable bounds and storage installation logic

3. Direct Full-Chronology Simulation Evaluation
for each generation $g = 1, \ldots, G_{max}$ do
for each candidate configuration x_k do
Apply the same storage siting and sizing configuration to all operating scenarios
Initialise the continuous storage SOC states
for each time step $t = 1, \ldots, T$ do
Select the normal- or adverse-weather source-load data according to the weather flag
Set the grid-connected or islanded operating mode according to the network-state flag
Determine storage charging/discharging power and served load
Run the pandapower AC power-flow calculation
Record node voltage, line loading, grid-interaction power, supplied load, and power losses
Update the storage SOC without resetting it at weather or network-mode transitions
end for
Calculate physical F_1, F_2 and F_3; pass $(-F_1, F_2/10^6, -F_3)$ to the minimisation-based optimiser.
Calculate the total constraint violation of x_k
end for
Perform constraint-dominance comparison and non-dominated sorting
Associate feasible individuals with the NSGA-III reference directions
Select parent individuals and generate offspring through crossover and mutation
Repair the offspring decision variables
end for

4. Pareto-Front Extraction
Collect all configurations evaluated using the full-chronology AC power-flow model
Remove configurations that violate the operational constraints. Perform non-dominated sorting on feasible configurations using $(-F_1, F_2/10^6, -F_3)$; report unscaled physical objectives.
Obtain the final feasible non-dominated approximation obtained within the evaluation budget
Export the storage locations, capacities, powers, objective values, constraint indicators, and Pareto-front figures

4. Results

4.1. Scenarios and Parameters

The IEEE 33-bus radial distribution network is the AC test system [21,22]. It contains 33 buses and 32 branches, with a nominal voltage of 12.66 kV and nominal active/reactive load totals of 3.715 MW and 2.300 Mvar. Network topology and electrical parameters follow MATPOWER case33bw. Bus 1 is the upstream reference only while connected; the islanded reference is provided by a BESS as specified in Section 2.3.3.

Buses 6, 12, 18, 25, and 31 host PV generation with a total installed capacity of 5 MW. Buses 8, 15, 22, 29, and 33 are candidate BESS sites, and buses 7, 13, 19, 26, and 32 are critical-load buses. In grid-connected operation, the controller prioritises reserve restoration to SOC 0.90 and voltage support; it does not actively discharge storage for peak–valley arbitrage. During islanding, PV and BESS supply the network subject to critical-load priority and the stated operating limits.

The case study is a PV–BESS AC microgrid. Wind turbines are not included in its generation portfolio. PV modules and BESS units connect through inverter interfaces to the IEEE 33-bus AC network. The BESS provides stored energy and inverter-limited active/reactive support, while the selected reference BESS establishes the steady-state islanded voltage and angle reference. PV forecasting results describe the generation input; storage sizing, SOC, voltage, and line-loading results describe the response of the integrated PV–BESS system.

The source-load time-series case is constructed by combining public models with typical load profiles. The baseline PV output follows the PV power calculation method of the NREL PVWatts model [23], is normalised, and is then scaled to the 5 MW installed capacity. The baseline load follows the hourly commercial and residential building load profiles published by NREL on the OpenEI/OEDI platform [24] and is proportionally adjusted to the 3.715 MW active-load base of the IEEE 33-bus system. These public data are used primarily to determine typical intraday PV and load profile shapes. The 8784 h source-load sequence used here is a normalised and scaled case-study data set rather than the original observations in the public data sets. Normal- and adverse-weather scenarios are then defined. PV output under normal weather retains a relatively smooth unimodal profile. The adverse-weather scenario is created by reducing effective irradiance and superimposing cloud disturbances, producing a lower peak and stronger short-term fluctuations in PV output.

The synthetic source–load dataset covers the 8784 h of leap year 2024. Its chronological partitions contain 6148 training hours (1 January 00:00–13 September 03:00), 1317 validation hours (13 September 04:00–7 November 00:00), and 1319 test hours (7 November 01:00–31 December 23:00). The storage-planning chronology is the complete independent test period. Forecasting models are not selected or tuned using that period. The 3.715 MW value is the nominal active-load base of the IEEE 33-bus system, not a claim that every simulated hour has that demand.

The adverse-weather profiles are synthetic and do not represent observations of a particular extreme-weather event. PV power is calculated from an adverse-weather irradiance indicator G_t^{adv} and temperature T_t as $P_{PV,t}^{adv} = \text{clip}\,[5G_t^{adv}(1 - 0.004(T_t - 25)), 0, 5]$ MW. A separate hourly synthetic load sequence and a severe-weather flag specify the associated demand and weather state. The archived irradiance indicator, disturbance sequence, and load realisation determine the actual scenario; the clipping equation alone does not uniquely reconstruct them. These scenario inputs therefore support a controlled methodological case study, rather than field validation of extreme-weather forecasting.

The baseline islanding event is selected from internal severe-weather events in the test chronology, excluding boundary events with incomplete operating transitions. Selection

prioritises the longest continuous event, then the largest cumulative positive net-load deficit, and finally the earliest start in a tie. The selected event lasts from 2 December 2024 00:00 to 3 December 23:00, corresponding to test-period indices 599–646 under zero-based indexing. Adverse-weather inputs are used during these 48 h; SOC is not reset at the transition into or out of islanded operation.

Figure 2 shows the IEEE 33-bus AC network, PV buses, candidate BESS buses, and critical-load buses. Bus 1 denotes the upstream connection; during islanding, the selected BESS, rather than the disconnected upstream source, provides the steady-state voltage and angle reference.

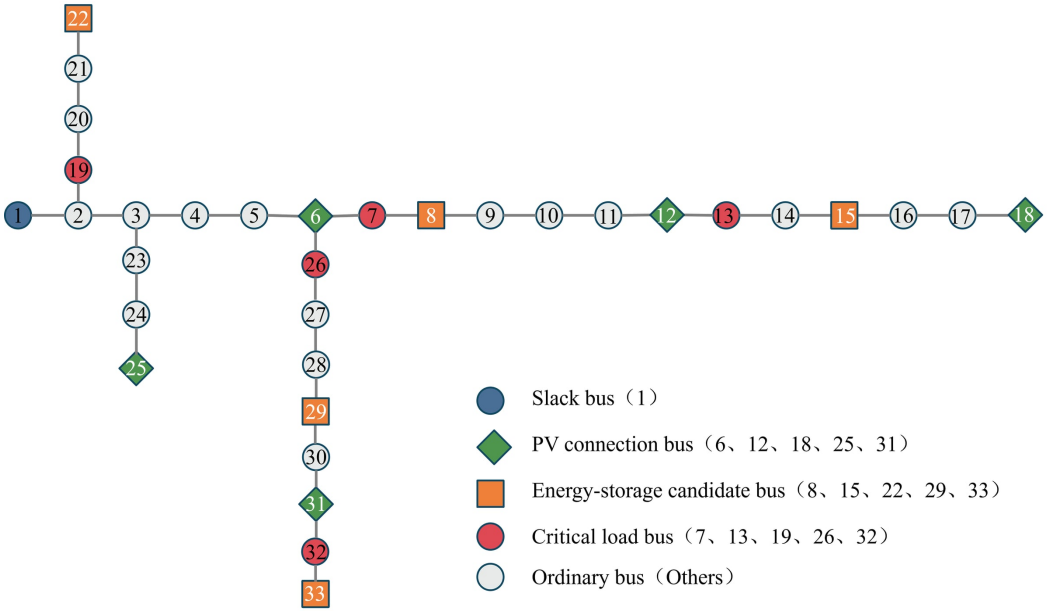


Figure 2. Configuration of the IEEE 33-bus microgrid scenario.

The case-study parameters are listed in Table 4.

Table 4. Case-study parameters.

Parameter	Value	Parameter	Value
Base voltage	12.66 kV [a]	Initial storage SOC	90% [g]
Base power	10 MVA [a]	Storage SOC limits	12–90% (case setting)
Total active load	3.715 MW [a]	Round-trip efficiency	90% [f]
Total reactive load	2.300 Mvar [a]	Nodal-voltage range	0.95–1.05 p.u. [b]
Total installed PV capacity	5 MW [g]	Rated active-power search range per installed BESS	0.20–2.20 MW
Maximum number of storage units	5 [g]	Islanding duration	48 h [g]
Minimum scheduled supply ratio	15% [g]	Critical-load supply ratio	100% [g]
Investment cost per unit capacity	RMB 1578/kWh [d]	Investment cost per unit power	RMB 678/kW [d]
Throughput-based O&M cost	RMB 0.05/kWh [c]	Economic horizon/discount rate	10 years/8% [e]
Off-peak/shoulder/peak purchase price	RMB 0.414/0.782/1.149 per kWh [d]	Sale price	RMB 0.550/kWh [d]

Note: network parameters and the power-flow implementation follow [21,22]; voltage limits follow [20]. Reference [25] motivates the literature-based 10–90% SOC range and throughput-cost proxy,

whereas the final case-study operating constraint is 12–90%. Unit investment costs and tariffs follow [12], economic horizon and discount rate follow [13], and round-trip efficiency follows [26]. The 0.20–2.20 MW rated-power search range, five candidate sites, 48 h event, reserve policy, and critical-load requirements are case-study settings. [a] IEEE 33-bus network data and the pandapower implementation follow [21,24]; [b] nodal-voltage limits follow [22]; [c] the storage SOC range and throughput-based operating-cost proxy follow [25]; [d] unit storage investment costs and electricity purchase/sale prices follow [12]; [e] the economic lifetime and discount rate follow [13]; [f] round-trip efficiency follows [26]; and [g] values are set according to the case-study scale, equipment search bounds, 48 h islanding event, and critipal-load supply requirement.

4.2. IGWO-GRU Performance Under Different Weather Scenarios

Figure 3 presents the PV output forecasts and error characteristics of IGWO-GRU under normal and adverse weather. Under normal weather, PV output is strongly periodic, and the forecast and actual curves agree closely at peaks, troughs, and ramping periods. Under adverse weather, both the frequency and magnitude of output fluctuations increase markedly, but the forecasts still track the principal variations, indicating that the model effectively identifies nonstationary sequences.

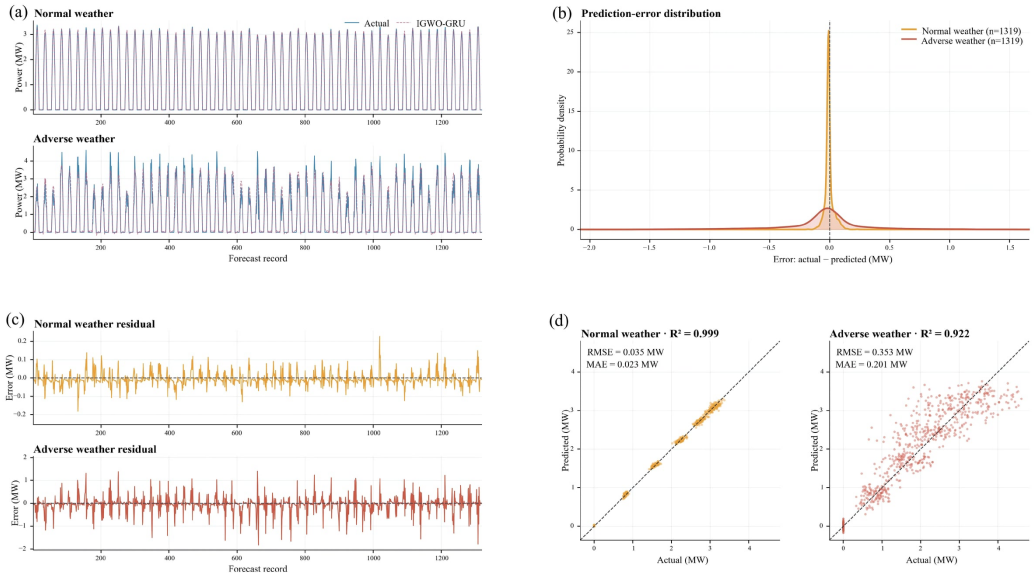


Figure 3. PV output forecasts under normal and adverse weather.

The displayed one-step PV errors are more concentrated around zero under normal weather and more dispersed under adverse weather. These distributions describe the representative prediction samples; they do not establish temporal independence or exclude sustained net-load errors over an islanding event. The planning-input comparison below directly assesses the consequences for storage adequacy.

For the representative adverse-weather PV forecast shown in Figure 3, R^2 = 0.921723901, which rounds to 0.922; the previous textual value of approximately 0.83 was a transcription error. This representative-run value is distinct from the repeated-training mean $R^2 = 0.9256 \pm 0.0028$ reported in Table 5. The synthetic reference profiles used in these comparisons are not field-measured operating data.

Table 5. Forecasting performance across five training runs.

Weather	Target	Model	RMSE (MW)	MAE (MW)	R^2
Normal	PV	Persistence	0.4128 ± 0.0000	0.2628 ± 0.0000	0.8858 ± 0.0000
Normal	PV	GRU	0.0414 ± 0.0042	0.0258 ± 0.0038	0.9988 ± 0.0002
Normal	PV	LSTM	0.0449 ± 0.0040	0.0278 ± 0.0026	0.9986 ± 0.0002
Normal	PV	GWO-GRU	0.0333 ± 0.0023	0.0199 ± 0.0028	0.9993 ± 0.0001
Normal	PV	IGWO-GRU	0.0398 ± 0.0056	0.0252 ± 0.0032	0.9989 ± 0.0003
Normal	Load	Persistence	0.0951 ± 0.0000	0.0710 ± 0.0000	0.9150 ± 0.0000
Normal	Load	GRU	0.0422 ± 0.0038	0.0350 ± 0.0036	0.9832 ± 0.0029
Normal	Load	LSTM	0.0514 ± 0.0058	0.0431 ± 0.0049	0.9749 ± 0.0054
Normal	Load	GWO-GRU	0.0348 ± 0.0060	0.0274 ± 0.0052	0.9884 ± 0.0042
Normal	Load	IGWO-GRU	0.0356 ± 0.0042	0.0286 ± 0.0032	0.9879 ± 0.0029
Adverse	PV	Persistence	0.6083 ± 0.0000	0.3659 ± 0.0000	0.7679 ± 0.0000
Adverse	PV	GRU	0.3471 ± 0.0053	0.1895 ± 0.0085	0.9244 ± 0.0023
Adverse	PV	LSTM	0.3502 ± 0.0047	0.1941 ± 0.0075	0.9230 ± 0.0021
Adverse	PV	GWO-GRU	0.3590 ± 0.0101	0.2052 ± 0.0208	0.9191 ± 0.0046
Adverse	PV	IGWO-GRU	0.3444 ± 0.0064	0.1872 ± 0.0083	0.9256 ± 0.0028
Adverse	Load	Persistence	0.1318 ± 0.0000	0.1039 ± 0.0000	0.8525 ± 0.0000
Adverse	Load	GRU	0.0858 ± 0.0016	0.0663 ± 0.0012	0.9375 ± 0.0024
Adverse	Load	LSTM	0.0942 ± 0.0046	0.0735 ± 0.0038	0.9245 ± 0.0075
Adverse	Load	GWO-GRU	0.0846 ± 0.0008	0.0666 ± 0.0009	0.9392 ± 0.0012
Adverse	Load	IGWO-GRU	0.0852 ± 0.0031	0.0665 ± 0.0023	0.9384 ± 0.0045

As shown in Figure 4, weather changes affect the regularity of the load sequence. Under normal weather, the load curve exhibits clear periodic fluctuations, and IGWO-GRU reproduces the load levels and peak-valley transitions in each period with small deviations from the actual values. Under adverse weather, local fluctuations increase because of the combined effects of weather and changes in consumer behaviour. The model nevertheless identifies the direction of load changes accurately and preserves the principal fluctuations in the actual sequence.

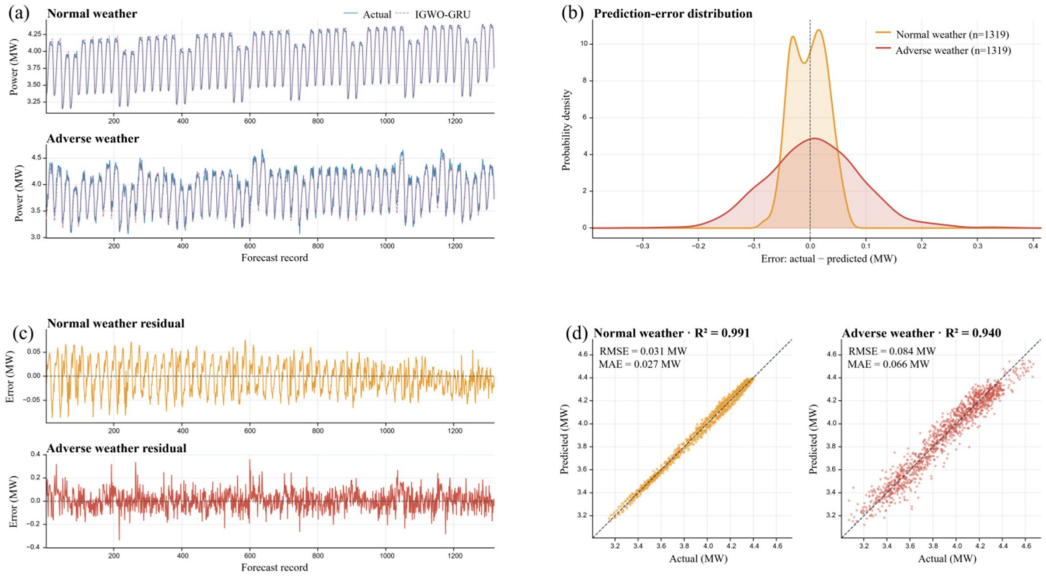


Figure 4. Load forecasts under normal and adverse weather.

The one-hour-ahead load error distributions shown in Figure 4 are concentrated near zero, with larger deviations in some adverse-weather samples. The representative scatter plots have R^2 values of approximately 0.99 and 0.94 under normal and adverse weather, respectively. These one-step scores do not establish that errors are independent across time or that cumulative energy-deficit errors are negligible for storage planning.

Table 5 compares persistence, GRU, LSTM, standard GWO-GRU, and IGWO-GRU using the same chronological partitions and task-specific inputs. Values for the learning-based models are means and standard deviations across five independent training runs. IGWO-GRU reduces mean RMSE relative to persistence by approximately 90.4%, 62.6%, 43.4%, and 35.4% for normal-weather PV, normal-weather load, adverse-weather PV, and adverse-weather load, respectively, using the displayed rounded values. It has the lowest mean RMSE and MAE and the highest mean R^2 for adverse-weather PV. Standard GWO-GRU has lower mean RMSE in the other three tasks. These results support competitive, scenario-dependent performance of the complete IGWO-GRU configuration, rather than universal superiority or a quantified contribution attributable to either search factor alone.

4.3. Energy Storage Siting and Sizing Results Considering an Islanding Event

The main planning experiment yielded 640 feasible configurations over the complete 1319 h chronology, including 10 non-dominated solutions, as shown in Figure 5. The physical objective directions are maximise F_1, minimise F_2, and maximise F_3. The resulting finite-budget Pareto approximation is conditional on the candidate buses, variable bounds and case-study chronology.

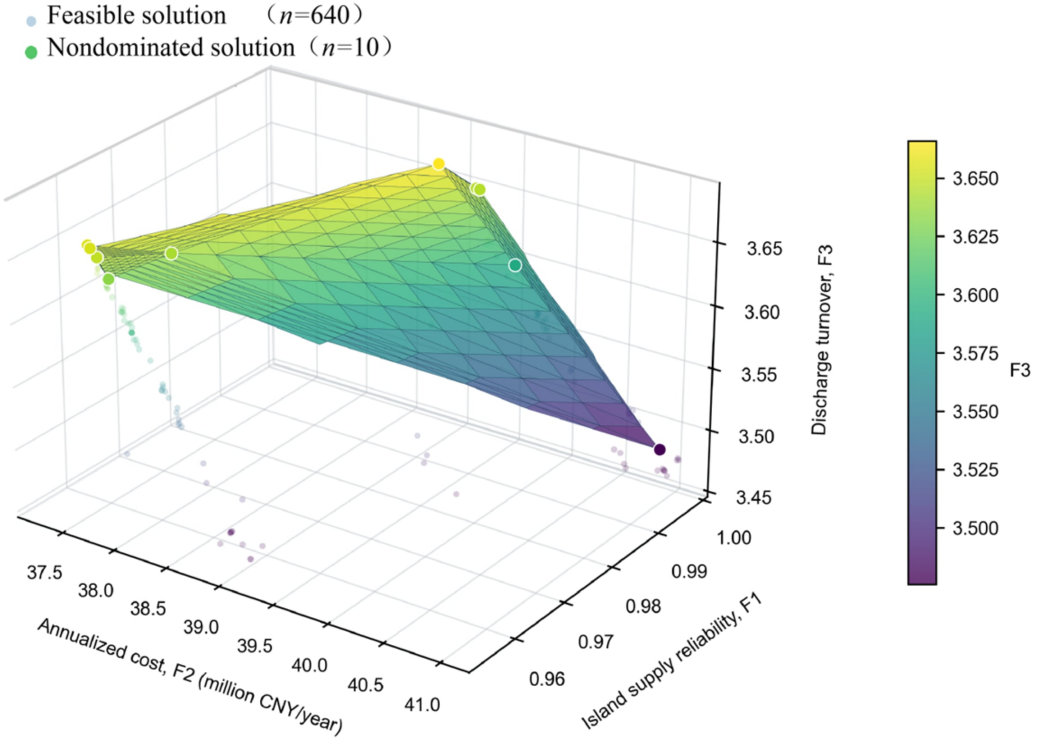


Figure 5. Storage siting and sizing solutions considering an islanding event (640 feasible configurations, including 10 non-dominated solutions).

Three representative non-dominated solutions are compared: economic-priority, balanced-compromise and full-load-supply. Their installed energy capacities are listed in Table 6. All three use buses 8, 15, 22, 29, and 33, which are the predefined candidate sites. Their reported total capacities are 144.377, 152.892, and 165.691 MWh, respectively. This case shows changes in capacity allocation with objective preference; it does not establish that each candidate site is indispensable.

Table 6. Representative installed energy capacities.

No.	Solution Type	Storage Capacity by Bus
1	Economic-priority	8 (30.617 MWh); 15 (32.586 MWh); 22 (18.792 MWh); 29 (31.911 MWh); 33 (30.471 MWh)
2	Balanced-compromise	8 (30.572 MWh); 15 (32.773 MWh); 22 (25.458 MWh); 29 (30.712 MWh); 33 (33.376 MWh)
3	Full-load-supply	8 (0.500 MWh); 15 (45.232 MWh); 22 (44.598 MWh); 29 (30.361 MWh); 33 (45.000 MWh)

The economic-priority solution has the lowest annualised cost among the three representative configurations and the smallest total installed energy. Its 18.792 MWh at bus 22 is lower than the allocations at the other four sites. It permits limited general-load curtailment during the baseline islanding event; its acceptability therefore depends on the decision maker's service requirements.

The balanced-compromise solution has 152.892 MWh installed energy, approximately 8.515 MWh (5.90%) more than the economic-priority solution. Much of this increment is assigned to buses 22 and 33; bus 22 increases from 18.792 to 25.458 MWh. This representative design is used for the subsequent operating illustration. Its choice reflects a reliability–cost–utilisation preference within the reported set, not a complete lifetime economic optimum.

The full-load-supply solution installs 165.691 MWh, approximately 14.76% more than the economic-priority solution and 8.37% more than the balanced-compromise solution. Buses 15, 22, and 33 each receive nearly 45 MWh, while bus 8 receives 0.500 MWh. These allocations are specific to the candidate set, search bounds and evaluated chronology.

The three representative configurations illustrate different preferences on the finite-budget Pareto approximation. Greater installed energy supports higher baseline supply reliability but increases cost and can reduce capacity utilisation. Selection among these designs requires an explicit service target and economic preference; the present objectives do not include a complete monetary valuation of interruption, degradation, or replacement.

Table 7 reports node-level capacities, rated powers, operating limits, and observed scheduled-power maxima for the balanced-compromise solution. Values are rounded for presentation; sums of displayed node entries may therefore differ slightly from the reported aggregate quantities. Column totals for the final two columns are simultaneous system maxima, not sums of individual maxima that may occur at different hours. Installed rated power is 9.961 MW, whereas maximum simultaneous scheduled charging and discharging are 3.000 and 3.721 MW.

Table 7. Node-level ratings and scheduled operating powers of the balanced-compromise solution.

Bus	Energy (MWh)	Rated P (MW)	Grid Limit (MW)	Island Schedule 0.95P (MW)	Inverter 1.20P (MVA)	Max. Charge (MW)	Max. Discharge (MW)
8	30.572	2	2	1.9	2.4	0.6	0.932
15	32.773	1.972	1.972	1.873	2.366	0.643	1.299
22	25.458	2	2	1.9	2.4	0.5	0.743
29	30.712	1.99	1.99	1.89	2.388	0.603	0.927
33	33.376	2	2	1.9	2.4	0.655	1.412
Total/system peak	152.892	9.961	9.961	9.463	11.954	3	3.721

Figure 6 corresponds to the balanced-compromise solution, with storage installed at buses 8, 15, 22, 29, and 33, a total capacity of 152.89 MWh, and a total power rating of 9.96 MW. The system supply metric is F_1 = 0.997032, corresponding to an aggregate load-

supply ratio of 99.7032% and an unserved proportion of only 0.2968%. Critical-load energy not supplied is 0 MWh, demonstrating that the optimised solution prioritises uninterrupted supply to critical loads.

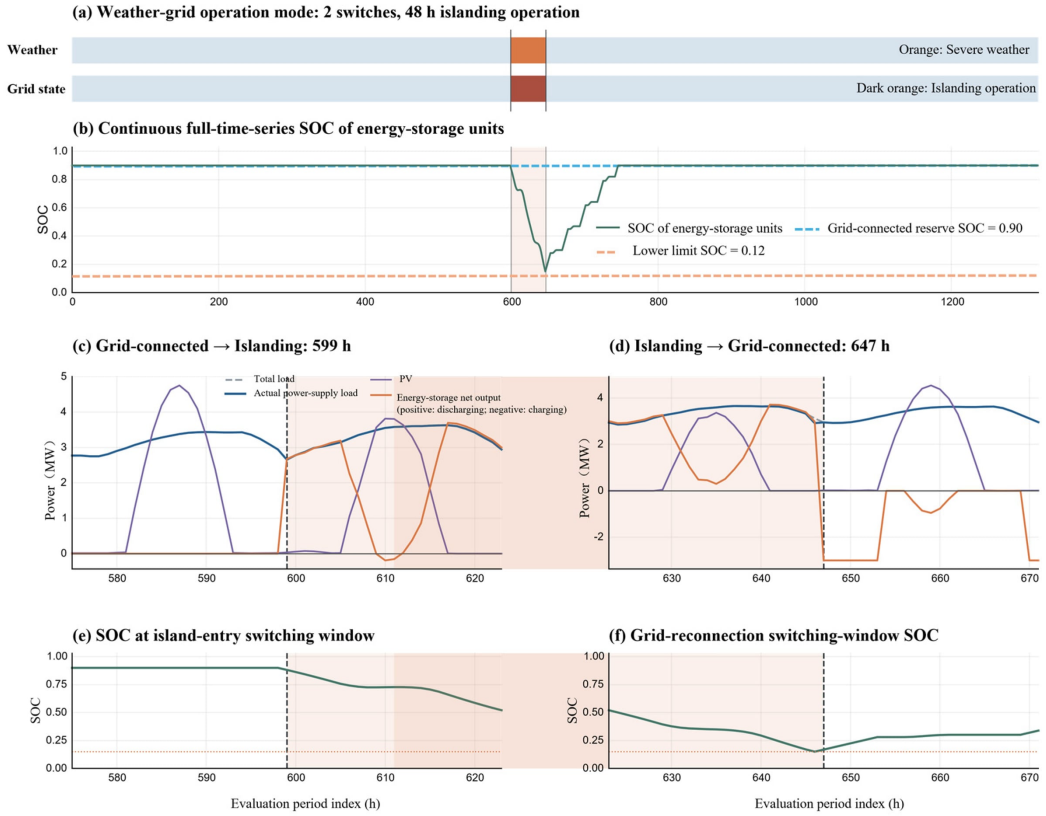


Figure 6. System power balance and storage SOC response during islanded operation.

The baseline islanding event comprises hourly steps 599–646 (zero-based indexing), corresponding to 2–3 December 2024; reconnection occurs at step 647. During islanding, upstream exchange is zero and PV, storage discharge, and permitted general-load curtailment maintain the modelled balance. SOC evolves continuously, and surplus PV can recharge storage when permitted by the operating limits.

For the reported final balanced-compromise configuration, the baseline feasibility assessment uses the 12–90% SOC constraint. The 48 h supply result is conditional on the specified source–load sequence, initial reserve, and steady-state network model. Post-event charging restores the reserve but also affects grid-connected cost and peak import, as quantified below.

The distributed solution balances islanded supply reliability, annualised cost, and capacity utilisation under the specified baseline event. Critical-load ENS is zero in that reported evaluation, while limited general-load curtailment remains. The additional tests below distinguish baseline feasibility from resilience under changed inputs and event timing.

4.3.1. Controlled Optimiser Comparison

A separate controlled comparison uses NSGA-III and NSGA-II with the same initial population, search bounds, operators and 640-evaluation budget. Each candidate is evaluated over the same 1319 h chronology. The minimisation objectives $(-F_1, F_2/10^6, -F_3)$ are normalised before indicator calculation. The non-dominated union of the compared feasible fronts defines a common empirical reference front for IGD. Table 8 and Figure 7 report the results under this comparison protocol; they are distinct from the main planning experiment, which yielded 640 feasible configurations, including 10 non-dominated solutions.

Table 8. Optimiser performance under the shared comparison protocol.

Algorithm	Evaluations	Runtime (min)	Final HV	Final IGD
NSGA-III	640	50.81	0.4051	0.0415
NSGA-II	640	51.46	0.4536	0.1648

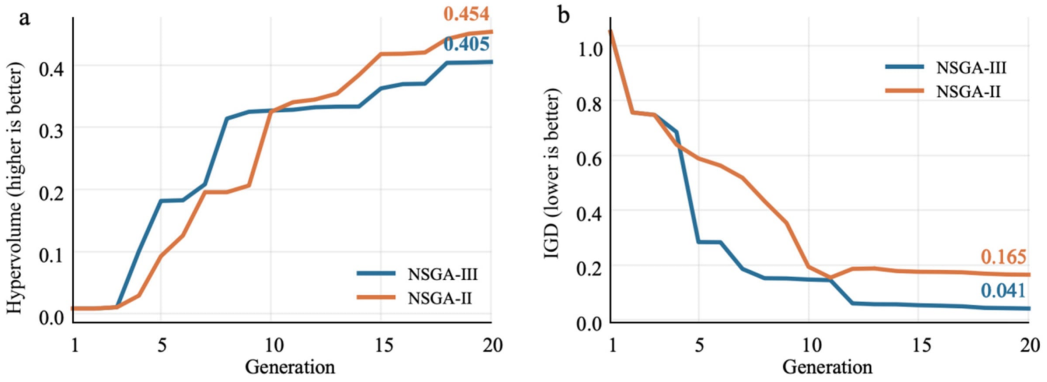


Figure 7. HV and IGD evolution under the shared NSGA-II/NSGA-III comparison protocol. (**a**) HV (**b**) IGD.

NSGA-II has approximately 12.0% higher final HV, whereas NSGA-III has approximately 74.8% lower IGD. Fifty of the 56 points in the common empirical non-dominated reference set originate from NSGA-III. The indicators therefore reveal complementary performance under the specified setting. Because the reference front is constructed from the compared solutions rather than a known global front, these results should not be interpreted as proof of global convergence or statistically general superiority.

A fixed-configuration input-sensitivity check also replaces the adverse-weather islanding forecasts with their normal-weather counterparts while retaining the 48 h event and the installed configurations. All 51 evaluated configurations satisfy the hard constraints under both inputs. Normal-weather inputs increase mean F_1 by 0.0031, reduce mean annualised cost by about RMB 70,300, and reduce mean F_3 by 0.323. This quantifies operational sensitivity to the source–load chronology; it is distinct from attributing separate causal contributions to forecasting, scenario construction and optimisation.

4.3.2. Influence of Planning Inputs

Three additional planning comparisons use forecast inputs, synthetic reference profiles, and eight representative joint PV–load typical days supplemented by a continuous 48 h extreme event. Candidate buses, operating constraints and the 640-evaluation budget are held fixed, and common scaling factors are used. Their representative solutions are evaluated against the same full 1319 h synthetic reference chronology in Table 9. These comparisons yield 9, 12, and 17 non-dominated solutions, respectively, and must not be confused with the main planning experiment. The reference inputs are synthetic values, not measured profiles.

Table 9. Planning inputs and evaluation on the common synthetic reference chronology.

Planning Input	Storage Nodes	Total Capacity (MWh)	Total Rated Power (MW)	Reliability Under Planning Input	Reliability Under Reference Chronology	Unserved Energy Under Reference Chronology (MWh)
Forecast-driven	8, 15, 22, 29, 33	149.451	9.954	1.0000	0.9390	8.906
Synthetic reference profiles	8, 15, 22, 29, 33	152.197	10.119	0.9500	0.9500	7.301
Typical days + extreme event	8, 15, 22, 29, 33	158.586	10.200	0.9827	0.9827	2.521

All three representative solutions use the same five candidate buses, while their capacities and rated powers differ. The reference-profile solution requires 2.746 MWh more energy capacity and 0.165 MW more rated power than the forecast-input solution. The latter has F_1 = 1.0000 under its own planning inputs but F_1 = 0.9390 and ENS = 8.906 MWh under the reference chronology, including 0.996 MWh of critical-load ENS and 3 h of interruption. Its voltage, line-loading, and SOC limits remain satisfied. The typical-day plus extreme-event solution increases capacity to 158.586 MWh and reduces reference-chronology ENS to 2.521 MWh. Forecast errors can therefore propagate into sizing and supply shortfalls even when site selection remains unchanged; global RMSE or R^2 alone does not guarantee reliable sizing for a prolonged event.

4.3.3. Storage Allocation and Grid-Connected Effects

The balanced-compromise solution's 152.892 MWh energy rating is determined by a prolonged energy deficit rather than the 3.715 MW nominal load base alone. The 90–12% SOC window provides 119.256 MWh before conversion losses, or approximately 113.136 MWh of AC discharge energy at $\eta_{dis} = \sqrt{0.90}$, before accounting for recharging and network losses. Table 10 compares this distributed configuration with no storage and a diagnostic centralised configuration placing the same aggregate energy and power at bus 33. The centralised diagnostic intentionally relaxes the distributed per-site 2.20 MW search bound to isolate spatial allocation.

Table 10. Diagnostic storage-allocation comparison.

Configuration	Storage Location	Capacity (MWh)	Rated Power (MW)	Energy-Dispatch F1	Minimum Voltage (p.u.)	Maximum Line Loading	Strictly Feasible
No storage	None	0	0	Islanded operation unavailable	0.9408 (grid-connected)	73.77% (grid-connected)	No
Centralised storage	Bus 33	152.892	9.961	0.997	0.8412	140.99%	No
Balanced-compromise	Buses 8, 15, 22, 29 and 33	152.892	9.961	0.997	0.9527	94.19%	Yes

Without storage, there is no modelled grid-forming source for islanding; the listed no-storage voltage and loading values are grid-connected results. The centralised diagnostic obtains F_1 = 0.997 at the energy-dispatch level but violates network constraints: minimum voltage is 0.8412 p.u., maximum line loading is 140.99%, and AC-corrected minimum SOC is 0.0624. The distributed solution remains feasible under the stated baseline conditions. Aggregate energy adequacy alone therefore does not establish network-feasible islanding.

Table 11 quantifies the grid-connected effects of the reserve-oriented controller. Distributed BESS raises minimum voltage from 0.9408 to 0.9550 p.u. and reduces annualised line losses by 69.24 MWh (4.27%). However, post-event recharge increases annualised net electricity cost by RMB 232,300 and peak upstream import from 3.895 to 7.110 MW. The evaluated chronology contains 120.872 MWh of grid-connected charging. These results support voltage and loss benefits, not a claim of peak shaving, energy arbitrage, or lower electricity-purchase cost.

Table 11. Grid-connected operating effects of the reserve-oriented BESS strategy.

Grid-Connected Indicator	No Storage	Balanced-Compromise	Change
Annualised electricity purchase/sale cost (RMB 10,000)	1253.74	1276.97	+23.23
Annualised line losses (MWh)	1620.22	1550.98	−69.24 (−4.27%)
Minimum nodal voltage (p.u.)	0.9408	0.9550	+0.0142
Maximum nodal voltage (p.u.)	1.0476	1.0450	−0.0026
Maximum line loading	73.77%	94.19%	+20.42 percentage points
Maximum upstream-grid import (MW)	3.895	7.110	+3.215

4.4. Sensitivity Analysis

Figure 8 presents a threshold sensitivity analysis for the fixed economic-priority, balanced-compromise and full-load-supply configurations. Each is evaluated over the complete 1319 h AC chronology while varying the specified operating parameter.

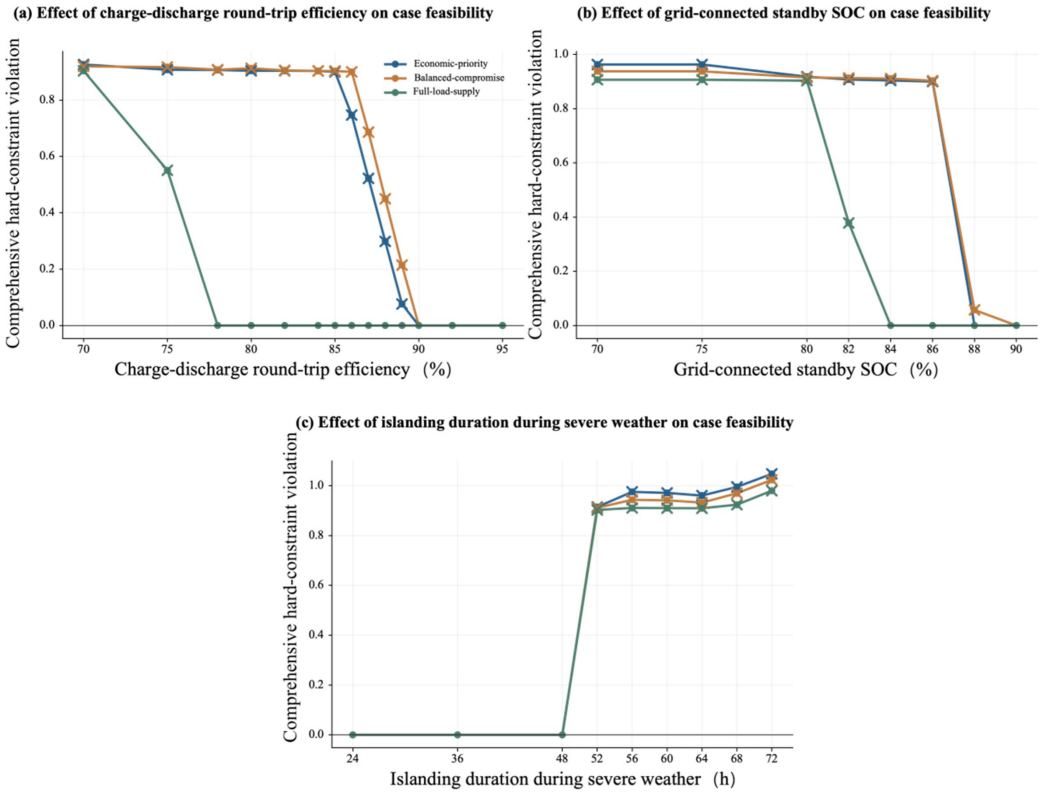


Figure 8. Threshold sensitivity analysis of key operating parameters for the solutions.

For charging/discharging-path efficiency, the economic and balanced-compromise solutions remain highly feasible when efficiency is at least approximately 90%; feasibility decreases rapidly once efficiency falls below the threshold. The minimum feasible efficiency

of the full-load-supply solution is approximately 78%, indicating that its larger storage capacity compensates for charging and discharging losses and makes it more tolerant of reduced efficiency.

Reserve storage SOC also exhibits clear threshold behaviour. The minimum feasible reserve SOC values of the economic and balanced-compromise solutions are approximately 88% and 90%, respectively, indicating that their relatively tight capacity allocations require high stored energy before islanding. The full-load-supply solution remains feasible when reserve SOC falls to approximately 84%, reflecting a larger energy margin. More abundant storage capacity thus increases tolerance to insufficient initial SOC.

For the original event start time, the duration sensitivity shows a marked feasibility transition near 48 h. This is a conditional threshold for that chronology, not an event-duration limit that applies independently of seasonal inputs or start time. The multi-event assessment below evaluates those additional dimensions.

The threshold analysis identifies case-specific sensitivity to conversion efficiency, pre-event SOC and event duration. Larger installed energy provides additional operating margins in some conditions, but none of these threshold results establishes generally sufficient control settings or lifetime robustness.

4.4.1. Fixed-Configuration Stress Tests

Additional fixed-configuration stress tests retain the three representative site, capacity and power allocations and repeat the chronological AC evaluation for the scenarios in Table 12. A strict-feasibility result of 0/3 means that each configuration violates at least one joint operating requirement; it does not mean that all supplied energy becomes zero. For example, the full-load-supply configuration retains F_1 = 1.0000 with a 6 h load-peak shift but reaches SOC 0.9106, exceeding the 0.90 upper limit. In the PV −5%, load +5% case, it retains F_1 = 0.9864 with zero critical-load ENS, while general-load supply and power-flow convergence violations still prevent strict feasibility.

Table 12. Islanded reliability and strict feasibility under changed operating conditions.

Scenario	Economic-Priority	Balanced-Compromise	Full-Load-Supply	Strictly Feasible
48 h baseline islanding	0.9578	0.9970	1.0000	3/3
24 h islanding	0.9576	0.9983	1.0000	3/3
72 h islanding	0.7751	0.8007	0.8387	0/3
PV −5%, load +5%	0.8975	0.9338	0.9864	0/3
PV −10%, load +10%	0.8416	0.8759	0.9264	0/3
Load peak shifted by 6 h	0.9583	0.9959	1.0000	0/3
Available capacity retention of 90%	0.8968	0.9307	0.9806	0/3
Available capacity retention of 80%	0.8343	0.8644	0.9092	0/3

The 72 h event, adverse source–load deviations and reduced available capacity cause substantial loss of supply reliability. Capacity-retention factors of 90% and 80% represent reduced available energy, not a cycle-dependent electrochemical ageing model. The results quantify the stress tolerance of the existing designs without re-optimising them; they do not establish lifetime feasibility or the cost of degradation and replacement.

4.4.2. Seasonal and Event-Duration Assessment

A fixed-configuration Monte Carlo assessment evaluates 60 islanding events sampled from the full 8784 h synthetic annual source–load dataset, separately from the main test-period planning experiment, stratified into 15 events in each season. Start times are sampled within the corresponding season. Event durations are drawn from 24, 36, 48, 60, and 72 h

with assumed probabilities 0.10, 0.20, 0.40, 0.20, and 0.10. Hourly AC feasibility and continuous SOC are re-evaluated for each installed configuration. Table 13 reports sample feasibility frequencies and supply-reliability summaries. These are conditional results under a specified synthetic stress distribution, not empirical outage probabilities.

Table 13. Results for the 60 sampled synthetic islanding events.

Configuration	Strict Feasibility	Mean F1	F1 Fifth Percentile	Critical-Load Shortfall Frequency
Economic-priority	85.00%	0.9516	0.8712	15.00%
Balanced-compromise	81.70%	0.9857	0.9066	15.00%
Full-load-supply	90.00%	0.9937	0.9549	10.00%

All three configurations are feasible for the sampled 24 h events. At 48 h, the feasibility frequencies are 96.4%, 92.9%, and 100% for economic-priority, balanced-compromise and full-load-supply, respectively; they decrease to 60%, 60%, and 80% at 60 h and to 50% for all three at 72 h. Winter is the most demanding sampled season, with respective frequencies of 73.3%, 73.3%, and 80.0%. Thus, 48 h is not an absolute failure boundary independent of event timing. The separate deterministic 52 h extension concerns the original start time, whereas the Monte Carlo assessment varies both timing and duration.

5. Discussion and Future Research

This study demonstrates pronounced diminishing marginal returns on storage-capacity investment. Moving from the economic-priority to the balanced-compromise solution increases annualised cost by RMB 1.4145 million and reduces energy not supplied by approximately 6.32 MWh. Moving further from the balanced-compromise to the full-load-supply solution increases cost by RMB 1.9698 million but reduces energy not supplied by only approximately 0.478 MWh. Improving from near-complete supply to strictly zero unserved energy therefore requires reserve capacity that is used infrequently, and its economic value depends on outage costs and reliability requirements.

A post-optimisation interruption-cost comparison retains the original Pareto configurations. If ν is the assumed number of comparable islanding events per year and v is VoLL in RMB/kWh, the conditional comparison adds 1000νvENS to annualised planning and operating cost. At $\nu = 1$, upgrading economic-priority to balanced-compromise increases annualised cost by about RMB 1.4145 million and reduces ENS by about 6.32 MWh, giving a break-even VoLL of approximately RMB 224/kWh. Upgrading further to full-load-supply costs about RMB 1.9698 million for an additional ENS reduction of about 0.478 MWh, giving approximately RMB 4.12×10^3/kWh. These rounded thresholds illustrate diminishing marginal benefit under the stated event-frequency assumption. VoLL is used for this conditional post-evaluation, not as an additional objective in the reported optimisation, and degradation/replacement costs remain excluded.

Capacity-normalised discharge throughput F_3 measures the sum of node-level AC discharge-to-capacity ratios over the complete chronology. Its higher value for the balanced-compromise configuration indicates greater utilisation, not greater physical conversion efficiency or improved battery health. The additional cycling exposure may increase ageing risk, whereas the lower-throughput full-load-supply configuration includes more reserve capacity. This objective must therefore be assessed jointly with reliability and cost.

All 10 Pareto solutions install storage at buses 8, 15, 22, 29, and 33, demonstrating how distributed deployment supports different feeder areas. Because the candidate set is limited to these buses and the model excludes fixed construction costs per site, however,

some solutions exhibit minimum-capacity "placeholders"; the results do not establish that all five sites are indispensable. In addition, the balanced-compromise SOC trajectory in Figure 6 approaches the lower operating limit of 0.12 near the end of islanding. Although this solution satisfies the baseline mathematical constraints, its limited remaining SOC margin indicates sensitivity to forecast errors, battery ageing, prolonged adverse weather, and equipment failures.

The results are methodological evidence for a synthetic PV–BESS IEEE 33-bus case. The limited candidate set, absence of fixed site-construction costs, synthetic weather and load processes, and assumed outage distribution restrict generalisation. Forecast scores are conditional on the provided meteorological inputs. The algorithm comparisons describe the specified shared evaluation protocol, and IGD uses an empirical rather than known global front. The finite scenario tests do not establish transient stability, frequency performance, black start, protection coordination, or lifetime economic optimality. These limitations motivate validation with measured inputs, operational weather forecasts, explicit ageing and replacement costs, and dynamic inverter models.

6. Conclusions

This paper proposed a source-load data-driven method for siting and sizing distributed energy storage in an islanded microgrid by integrating IGWO-GRU source-load forecasting, pandapower full-chronology AC power flow, and NSGA-III multi-objective optimisation. The same storage configuration was used continuously across normal weather, adverse weather, and transitions between grid-connected and islanded operation. The objectives were islanded supply reliability, planning and operating cost, and capacity-normalised discharge throughput. During optimisation, a complete chronological power-flow calculation was performed directly for every candidate, and all objective values and constraint metrics were obtained from the actual calculation results.

For the IEEE 33-bus case, complete 1319 h chronological evaluations yielded 640 feasible configurations, including 10 non-dominated solutions. The islanded supply reliability of the Pareto solutions ranged from 0.958 to 1.000, the annualised planning and operating cost ranged from RMB 37.4617 million/year to RMB 40.8460 million/year, and capacity-normalised discharge throughput ranged from 3.4758 to 3.6658. All non-dominated solutions achieved zero unserved energy at critical buses, maintained nodal voltages within 0.953–1.045 p.u., and limited the maximum line loading to 96.9503%, verifying their power-flow feasibility under the specified operating scenarios.

The representative configurations show the reliability–cost–utilisation trade-off. The economic-priority solution installs 144.377 MWh and permits limited general-load curtailment. The balanced-compromise solution installs 152.892 MWh, increases baseline F_1 from approximately 0.958 to 0.997 at a 3.78% annualised cost premium, and has the highest F_3 among the reported designs. The full-load-supply solution installs 165.691 MWh and supplies all loads throughout the specified baseline 48 h event, at higher cost and lower utilisation. These are conditional case-study outcomes; selecting a design requires a service target, an economic preference, and consideration of the omitted lifetime costs.

The results also show that islanded supply capability in this case is governed primarily by energy reserves during sustained adverse weather rather than instantaneous discharge-power limits. As supply reliability increases, total storage capacity rises markedly, whereas total power does not increase in parallel. Sensitivity analysis further identifies feasibility thresholds for round-trip efficiency, pre-event reserve SOC, and islanding duration. Extending the islanding period from 48 to 52 h causes constraint violations in all three representative solutions, indicating that the planning conclusions have explicit scenario-dependent applicability limits.

Author Contributions: Methodology, J.C., H.Y., T.Z., G.W., and Z.W.; validation, J.C.; investigation, J.C., H.Y., T.Z., G.W., Z.W., J.S., Y.W., and G.S.; writing—original draft preparation, J.C.; writing—review and editing, G.Z. and Y.Y.; funding acquisition, J.C., H.Y., T.Z., G.W., Z.W., J.S., Y.W., and G.S. All authors have read and agreed to the published version of the manuscript.

Funding: This work was supported by the Science and Technology Project of State Grid Anhui Electric Power Co., Ltd. under Grant Nos. AHDLKJXMRWS2025148 and B312J0250009, "Research on Flexible Interactive Control Technology for Distribution Networks Oriented to the Adaptive Integration of Large-Scale Distributed Resources".

Institutional Review Board Statement: Not applicable.

Informed Consent Statement: Not applicable.

Data Availability Statement: The public modelling references are PVWatts [23], NREL building-load profiles [24], the IEEE 33-bus test system [21] and pandapower [22]. The derived 8784 h source–load sequence and Pareto solution files are not publicly available because of the funding project's confidentiality requirements. The chronological partitions, model settings, scenario-selection rule and summary results are reported to clarify the evaluation procedure. Exact numerical reconstruction also depends on the archived synthetic input realisations and computational records; the public modelling references alone do not uniquely determine the reported case-study dataset.

Conflicts of Interest: Authors Jianfang Chen, Tao Zhou, Guansen Wang, Zhong Wang, Jianming Su were employed by the company State Grid Anhui Electric Power Co., Ltd. Tongling Power Supply Company, Tongling, China; Haijun Yu was employed by the company State Grid Anhui Electric Power Co., Ltd., Hefei, China. The remaining authors declare that the research was conducted in the absence of any commercial or financial relationships that could be construed as a potential conflict of interest.

References

1. Lasseter, R.H. MicroGrids. In Proceedings of the 2002 IEEE Power Engineering Society Winter Meeting, New York, NY, USA, 27–31 January 2002; Volume 1, pp. 305–308. [CrossRef]
2. Lopes, J.A.P.; Moreira, C.L.; Madureira, A.G. Defining control strategies for MicroGrids islanded operation. *IEEE Trans. Power Syst.* **2006**, *21*, 916–924. [CrossRef]
3. Yang, J.; Su, C.Q. Robust optimization of microgrid based on renewable distributed power generation and load demand uncertainty. *Energy* **2021**, *223*, 120043. [CrossRef]
4. Bhuiyan, F.A.; Yazdani, A.; Primak, S.L. Optimal sizing approach for islanded microgrids. *IET Renew. Power Gener.* **2015**, *9*, 166–175. [CrossRef]
5. El-Bidairi, K.S.; Nguyen, H.D.; Mahmoud, T.S.; Jayasinghe, S.; Guerrero, J.M. Optimal sizing of battery energy storage systems for dynamic frequency control in an islanded microgrid: A case study of Flinders Island, Australia. *Energy* **2020**, *195*, 117059. [CrossRef]
6. Sitompul, S.; Fujita, G. Impact of advanced load-frequency control on optimal size of battery energy storage in islanded microgrid system. *Energies* **2021**, *14*, 2213. [CrossRef]
7. Takano, H.; Hayashi, R.; Asano, H.; Goda, T. Optimal sizing of battery energy storage systems considering cooperative operation with microgrid components. *Energies* **2021**, *14*, 7442. [CrossRef]
8. Su, R.; He, G.B.; Su, S.; Duan, Y.; Cheng, J.; Chen, H.; Wang, K.; Zhang, C. Optimal placement and capacity sizing of energy storage systems via NSGA-II in active distribution network. *Front. Energy Res.* **2023**, *10*, 1073194. [CrossRef]
9. Gu, T.M.; Wang, P.Y.; Liang, F.Y.; Xie, G.; Guo, L.; Zhang, X.-P.; Shi, F. Placement and capacity selection of battery energy storage system in the distributed generation integrated distribution network based on improved NSGA-II optimization. *J. Energy Storage* **2022**, *52*, 104716. [CrossRef]
10. Yang, F.; Hu, Y.; Zhang, L.; Xu, Z.; Wu, W.; Gu, W. Siting and sizing of distributed energy storage in a distribution network considering uncertainty in islanding duration. *J. Electr. Power Sci. Technol.* **2023**, *38*, 43–54. [CrossRef]
11. Murshed, M.; Chamana, M.; Schmitt, K.E.K.; Pol, S.; Adeyanju, O.; Bayne, S. Sizing PV and BESS for grid-connected microgrid resilience: A data-driven hybrid optimization approach. *Energies* **2023**, *16*, 7300. [CrossRef]
12. Zhi, H.Q.; Guo, X.Y.; Chang, X.; Hao, L. A study on the dual-layer energy storage configuration in photovoltaic distribution networks considering voltage-loss synergy optimisation. *Front. Energy Res.* **2026**, *14*, 1718662. [CrossRef]

13. Wu, G.L.; Lin, J.; Liao, J.L. A dual-layer planning method based on improved MOPSO for distribution networks considering source-load temporal uncertainty. *Front. Energy Res.* **2025**, *13*, 1598553. [CrossRef]
14. Kong, W.C.; Dong, Z.Y.; Jia, Y.W.; Hill, D.J.; Xu, Y.; Zhang, Y. Short-term residential load forecasting based on LSTM recurrent neural network. *IEEE Trans. Smart Grid* **2019**, *10*, 841–851. [CrossRef]
15. Tang, Y.G.; Yang, K.; Zhang, S.J.; Zhang, Z. Photovoltaic power forecasting: A dual-attention gated recurrent unit framework incorporating weather clustering and transfer learning strategy. *Eng. Appl. Artif. Intell.* **2024**, *130*, 107691. [CrossRef]
16. Mirjalili, S.; Mirjalili, S.M.; Lewis, A. Grey wolf optimizer. *Adv. Eng. Softw.* **2014**, *69*, 46–61. [CrossRef]
17. Chen, Q.M.; Liao, H.F.; Sun, Y.K.; Zeng, Y.S. Photovoltaic power forecasting model based on GWO-GRU. *Acta Energiae Solaris Sin.* **2024**, *45*, 438–444. [CrossRef]
18. Nadimi-Shahraki, M.H.; Taghian, S.; Mirjalili, S. An improved grey wolf optimizer for solving engineering problems. *Expert Syst. Appl.* **2021**, *166*, 113917. [CrossRef]
19. McKay, M.D.; Beckman, R.J.; Conover, W.J. A comparison of three methods for selecting values of input variables in the analysis of output from a computer code. *Technometrics* **1979**, *21*, 239–245. [CrossRef]
20. Wang, J.X.; Zhang, S.D.; Sun, Y.H.; Du, X.; Wu, P.; Mahfoud, R.J. Day-ahead optimal dispatch for active distribution network considering probability model of controllable distributed generation. *Front. Energy Res.* **2022**, *9*, 814850. [CrossRef]
21. Baran, M.E.; Wu, F.F. Network reconfiguration in distribution systems for loss reduction and load balancing. *IEEE Trans. Power Deliv.* **1989**, *4*, 1401–1407. [CrossRef]
22. Thurner, L.; Scheidler, A.; Schäfer, F.; Menke, J.-H.; Dollichon, J.; Meier, F.; Meinecke, S.; Braun, M. Pandapower—An open-source Python tool for convenient modeling, analysis, and optimization of electric power systems. *IEEE Trans. Power Syst.* **2018**, *33*, 6510–6521. [CrossRef]
23. Dobos, A.P. *PVWatts, Version 5 Manual*; NREL/TP-6A20-62641; National Renewable Energy Laboratory: Golden, CO, USA, 2014. [CrossRef]
24. Ong, S.; Clark, N. *Commercial and Residential Hourly Load Profiles for all TMY3 Locations in the United States*; National Renewable Energy Laboratory: Golden, CO, USA, 2014. [CrossRef]
25. Wang, W.D.; Wang, H.Y.; Sun, S.B.; Cao, G.; Wang, S.; Ji, Y. Optimal configuration of shared energy storage for industrial users considering lifetime and charge-discharge strategy coupling. *Front. Energy Res.* **2024**, *12*, 1510259. [CrossRef]
26. Tesla. Powerwall Specifications. Available online: https://energylibrary.tesla.com/docs/Public/EnergyStorage/Powerwall/2/InstallManual/BackupGateway/2/en-us/GUID-05D2F038-D8E2-45AF-9F8C-7A3076858433.html (accessed on 17 September 2026).

Disclaimer/Publisher's Note: The statements, opinions and data contained in all publications are solely those of the individual author(s) and contributor(s) and not of MDPI and/or the editor(s). MDPI and/or the editor(s) disclaim responsibility for any injury to people or property resulting from any ideas, methods, instructions or products referred to in the content.